

Article

Iron Oxides Nanoparticles as Components of Ferroptosis-Inducing Systems: Screening of Potential Candidates

Artur Dzeranov ^{1,2,*}, Lyubov Bondarenko ^{1,*}, Denis Pankratov ³, Mikhail Prokof'ev ¹, Gulzhian Dzhardimalieva ^{1,4}, Sharipa Jorobekova ⁵, Nataliya Tropkaya ^{1,2}, Ludmila Telegina ⁶ and Kamila Kydralieva ¹

¹ Moscow Aviation Institute (National Research University), Moscow 125993, Russia

² Sklifosofskiy Research Institute of Emergency Medicine, Moscow 129010, Russia

³ Department of Chemistry, Lomonosov Moscow State University, Moscow 119991, Russia

⁴ Federal Research Center of Problems of Chemical Physics and Medicinal Chemistry, Russian Academy of Sciences, Chernogolovka 142432, Moscow region, Russia

⁵ Institute of Chemistry and Phytotechnologies, National Academy of Sciences, Bishkek 720071, Kyrgyzstan

⁶ Russian Institute for Scientific and Technical Information, Moscow 125190, Russia

* Correspondence: arturdzeranov99@gmail.com (A.D.); l.s.bondarenko92@gmail.com (L.B.)

Abstract: This study presents an analysis of a set of iron oxides nanoparticles (NPs) (γ -Fe₂O₃, α -FeOOH, δ -FeOOH, 5Fe₂O₃·9H₂O, and Fe₃O₄) as potential candidates for ferroptosis therapy in terms of a phase state, magnetic characteristics, and the release of Fe²⁺/Fe³⁺ as ROS mediators. Due to the values of saturation magnetization for Fe₃O₄ (31.6 emu/g) and γ -Fe₂O₃ (33.8 emu/g), as well as the surface area of these particles (130 and 123 m²/g), it is possible to consider them as promising magnetically controlled carriers that can function with various ligands. The evaluation of the release of Fe²⁺/Fe³⁺ ions as catalysts for the Fenton reaction showed that the concentration of the released ions increases within first 3 h after suspension and decreases within 24 h, which probably indicates desorption and adsorption of ions from/onto the surface of nanoparticles regardless their nature. The concentration of ions released by all nanoparticles, except α -FeOOH-Fe²⁺, reached 9.1 mg/L for Fe³⁺ to 1.7 mg/L for Fe²⁺, which makes them preferable for controlling the catalysis of the Fenton reaction. In contrast, a high concentration of iron ions to 90 mg/L for Fe³⁺ and 316 mg/L for Fe²⁺ released from compound α -FeOOH-Fe²⁺ allows us to utilize this oxide as an aid therapy agent. Results obtained on iron oxide nanoparticles will provide data for the most prospective candidates that are used in ferroptosis-inducing systems.

Keywords: ferroptosis-inducing systems; iron oxide nanoparticles; phase state; specific surface; magnetic properties; ferrous and ferric ions release



Citation: Dzeranov, A.; Bondarenko, L.; Pankratov, D.; Prokof'ev, M.; Dzhardimalieva, G.; Jorobekova, S.; Tropkaya, N.; Telegina, L.; Kydralieva, K. Iron Oxides Nanoparticles as Components of Ferroptosis-Inducing Systems: Screening of Potential Candidates.

Magnetochemistry **2023**, *9*, 3.

<https://doi.org/10.3390/magnetochemistry9010003>

<https://doi.org/10.3390/magnetochemistry9010003>

Academic Editor: Zheng Gai

Received: 15 November 2022

Revised: 13 December 2022

Accepted: 20 December 2022

Published: 23 December 2022



Copyright: © 2022 by the authors. Licensee MDPI, Basel, Switzerland. This article is an open access article distributed under the terms and conditions of the Creative Commons Attribution (CC BY) license (<https://creativecommons.org/licenses/by/4.0/>).

1. Introduction

The iron-based nanoparticles have become widely used in cancer therapy research thanks to the special physical and chemical properties of nanomaterials. Ferroptosis is a new iron-dependent form of programmed cell death, first described in 2012 by Dixon, and it is one of the types of regulated cell deaths caused by strong activation of lipid peroxidation, which depends on the formation of reactive oxygen species (ROS) and the availability of iron in cells [1,2]. Currently, ferroptosis-inducing systems initiate the Fenton reaction and overexpression of H₂O₂ in a cancer cell [3,4] as well as the subsequent formation of hydroxyl radicals (OH, one of the most toxic types of ROS) complexes [5–7]. In addition, various nanoplatforms based on iron (II, III) [3,8–10] are used, including ferromagnetic nanoparticles (maghemite γ -Fe₂O₃ or magnetite Fe₃O₄) [11,12] and complexes or their nanocomposites [13,14]. To our best knowledge, there have never been works devoted to the comparative evaluation of various iron-containing compounds as ferroptosis catalysts.

One of the factors affecting the Fenton reaction is the type of iron ions inducing the Fenton reaction by Fe^{3+} or the $\text{Fe}^{2+}/\text{Fe}^{3+}$ pair. The Fenton reaction is catalyzed by Fe^{2+} , and the Fenton-mediated reaction is catalyzed by Fe^{3+} ; both of them result in the production of toxic reactive oxygen species. In 1987, Minotti et al. showed [15] that lipid peroxidation can be induced both by the participation of separate Fe^{2+} or Fe^{3+} through the formation of hydroxyl radicals as a result of the Fenton reaction and with the participation of a pair of $\text{Fe}^{2+}/\text{Fe}^{3+}$ at once. Thus, He et al. (2020) obtained a lipid peroxidation catalyst containing a pair of $\text{Fe}^{2+}/\text{Fe}^{3+}$, where Fe^{2+} was reduced from Fe^{3+} by glutathione, an antioxidant enzyme found in high concentrations in cancer cells [16]. The authors reported the antitumor activity of the catalysts prepared in vitro and in vivo experiments against MCF-7/ADR breast cancer cells, MCF-7 breast cancer cells, 4T1 mouse breast cancer cells, and human liver cancer L02 cells without side effects. However, the resulting nanocatalysts cannot be used for targeted delivery due to the lack of magnetic properties, Huo et al., 2017 [12] showed that in the absence of an external magnetic field or any other methods of targeting the drug, only 6.95% of Fe_3O_4 with glucose oxidase in mesoporous silica framework accumulated in the tumor in 48 h. It is important to mention that there are no papers devoted to the comparative analysis of various iron-containing preparations that could catalyze the Fenton reaction. However, the authors of most publications related to the topic do not make a direct correlation between the concentration of released iron ions, the concentration of hydroxyl radicals, and the percentage of cell death. The use of iron oxide nanoparticles, in particular magnetite Fe_3O_4 and maghemite $\gamma\text{-Fe}_2\text{O}_3$, is the most widely used since (1) magnetite Fe_3O_4 nanoparticles contain both Fe^{2+} and Fe^{3+} ; (2) $\gamma\text{-Fe}_2\text{O}_3$ nanoparticles are the source of Fe^{3+} ions, which can be reduced to Fe^{2+} with ascorbic acid; and (3) Fe_3O_4 magnetite nanoparticles, like $\gamma\text{-Fe}_2\text{O}_3$ nanoparticles, have magnetic properties that provide the means to control them with the application of an external magnetic field.

An open issue in the design of iron preparations is the issue with the capability of the controlled induction of ROS in sufficient quantities in Fenton reactions to kill a cancer cell. It needs a high drug load, high yield, and controlled release of Fe^{2+} and Fe^{3+} ions; targeted delivery of the drug to the tumor; surface modification to control the “fate” in vivo and ensure stability; and effective detection using imaging techniques.

This study aimed to evaluate various types of bare iron oxide nanoparticles to be a core and iron ion source of nanosystems inducing reactive oxygen species (ROS) in terms of their phase state, magnetic properties, kinetics, and release concentration of ferrous and ferric ions. Iron oxide nanoparticles, nanoparticles of magnetite Fe_3O_4 , and maghemite $\gamma\text{-Fe}_2\text{O}_3$ were chosen as samples due to superparamagnetic properties [17,18], ferrihydrite $\delta\text{-FeOOH}$, due to a large specific surface [19] and a significant number of surface $-\text{OH}$ groups [20], and a good water solubility as well, ferrihydrite $5\text{Fe}_2\text{O}_3 \cdot 9\text{H}_2\text{O}$ and goethite $\alpha\text{-FeOOH}$ were chosen due to high reactivity with respect to dissolved organic substances [21–23] and a highly hydrated structure.

The use of different iron nanoparticles in order to search for effective iron preparations usually fails to achieve the desired properties using one universal preparation. On the contrary, the use of a set of iron nanoparticle preparations with subsequent analysis of the phase composition, magnetic characteristics, and surface characteristics determines the effectiveness of their use.

2. Materials and Methods

2.1. Chemicals

$\text{FeCl}_3 \cdot 6\text{H}_2\text{O}$ (Brom, Russia), $\text{FeSO}_4 \cdot 7\text{H}_2\text{O}$ (Chemicals, Russia), 10% NaOH (Kaustik, Russia), 30% H_2O_2 (Lega, Russia), $(\text{NH}_4)_2\text{Fe}(\text{SO}_4)_2 \cdot 6\text{H}_2\text{O}$ (MZKhR, Russia), NaBH_4 (Chemical Line, Russia). All reagents were chemically pure.

2.2. Preparation of Fe_3O_4

Magnetite Fe_3O_4 nanoparticles were prepared by the coprecipitation of aqueous solutions of iron (3+) and (2+) salts in the presence of alkali according to the Elmor method [24].

For that, 11.5 g of $\text{FeCl}_3 \cdot 6\text{H}_2\text{O}$ and 6 g of $\text{FeSO}_4 \cdot 7\text{H}_2\text{O}$ were dissolved in 0.5 L of deionized H_2O . The solution was heated to 60 °C. While stirring on a mechanical stirrer (1000 rpm), 10% NaOH was added to pH 10. The resulting precipitate of magnetite was separated from the solution using a magnet (Nd; 0.3 T) and applying it to the wall of the reaction flask. To remove Na^+ , Cl^- , SO_4^{2-} , and OH^- , the precipitate was washed 3 times with deionized water to pH~8. The sample was dried in a convector drier at 50 °C.

2.3. Preparation of $\gamma\text{-Fe}_2\text{O}_3$

A total of 10 g of maghemite nanoparticles was obtained by air-oxidation of a sample of magnetite nanoparticles in 20 mL 30% H_2O_2 in 5 days. The suspension was centrifuged within 10 min at 3000 rpm. The formulated nanoparticles were twice washed with deionized water and centrifuged (10 min, 3000 rpm). The sample was dried in the thermostat (105 °C, 24 h).

2.4. Preparation of $\delta\text{-FeOOH}$

One-step synthesis of $\delta\text{-FeOOH}$ was performed according to the method used by Pinto et al. [25]. A total of 400 mL of a solution containing 11 g of $(\text{NH}_4)_2\text{Fe}(\text{SO}_4)_2 \cdot 6\text{H}_2\text{O}$ was stirred on a mechanical stirrer (500 rpm, 10 min), and 150 mL of 10% NaOH was gradually added. A green suspension was formed. Thereafter, 5 mL of 30% H_2O_2 was immediately added, and a reddish brown precipitate was formed subsequently. The resulting solid precipitate was separated by centrifugation (10 min, 3000 rpm). The precipitate was washed with 800 mL of deionized water to pH ~8 and centrifuged (10 min, 3000 rpm). The sample was dried in a convector drier at 50 °C for 24 h.

2.5. Preparation of $5\text{Fe}_2\text{O}_3 \cdot 9\text{H}_2\text{O}$

Ferrihydrite NPs ($5\text{Fe}_2\text{O}_3 \cdot 9\text{H}_2\text{O}$) were obtained according to [26] as follows: 21.6 g of $\text{FeCl}_3 \cdot 6\text{H}_2\text{O}$ was dissolved in 400 mL of deionized water and then titrated with 1 M NaOH solution to pH~7.0 by continuous stirring (600 rpm) in a magnetic stirrer. The 0.1 M NaOH was adjusted to pH = 7.5 to form dark red solid ferrihydrite. The resulting solid was separated by centrifugation (20 min, 3000 rpm). The precipitate was washed with 400 mL of deionized water to pH = 6 and centrifuged (20 min, 3000 rpm). The sample was dried in a convector drier at 50 °C within 24 h.

2.6. Preparation of $\alpha\text{-FeOOH-Fe}^{2+}$

Due to the need to dope $\alpha\text{-FeOOH}$ by Fe^{2+} and prevent rapid oxidation to ferrihydrite, preparation of $\alpha\text{-FeOOH-Fe}^{2+}$ was adopted from [27] with modification: synthesis environment was changed from inert on ambient conditions and MeOH on EtOH.

An amount of 15 g $\text{FeSO}_4 \cdot 7\text{H}_2\text{O}$ was dissolved in 600 mL 70% deionized water and 30% ethanol. Using 1 M NaOH, the pH of the solution was adjusted to 6.8. Then a solution of sodium borohydride (3.8 g NaBH_4 in 150 mL) was added at a rate of 2 drops/s with constant stirring on a mechanical stirrer for 30 min (pH = 7.4). The solution was centrifuged (10 min, 3000 rpm). A yellow precipitate formed was washed twice with ethanol (200 mL each) and centrifuged (10 min, 3000 rpm). The resulting particles were dried in the thermostat (105 °C, 24 h).

2.7. Characterization

X-ray phase analysis was performed on Thermo Fisher Scientific ARL X'TRA diffractometer (Cu $\text{K}\alpha$ radiation ($\lambda = 1.54184 \text{ \AA}$) in the angle range $2\theta = 5\text{--}80^\circ$ at a scanning speed of 5 deg/min and 25 °C. Powder X-ray analysis was performed using Match! software. Mössbauer spectra with a noise/signal ratio of no more than 2% were obtained on an MS1104EM spectrometer using ^{57}Co in an Rh matrix as a source of gamma radiation, with a temperature control accuracy of ± 2 and 0.5 deg. for 295 and 77 K, respectively. The experimental spectra were interpreted using SpectRelax 2.8. The isomer shift was determined relative to $\alpha\text{-Fe}$.

The specific surface area and characteristics of the porous structure of the samples were determined on a Sorptometer-M sorptometer (Katakon, Russia) at liquid nitrogen temperature (77 K). The calculation of the specific surface area and characteristics of the porous structure of the samples based on the adsorption-desorption isotherms was carried out by using the Brunauer–Emmett–Teller (BET) and Barrett–Joyner–Halenda (BJH) methods. Before the start of the tests, the samples were degassed by heating in a He (helium) current, 150 °C, 2 h, flow rate 0.2 L/h in order to remove adsorbed gasses and vapors from the surface.

The magnetic properties of iron NPs were determined by using the VSM M4500 vibrating magnetometer (EG&G PARC, Gaithersburg, Maryland, USA) calibrated using a standard pure nickel sample (weighing 90 mg) with a relative accuracy of 1×10^3 at room temperature. During the experiment, the value of the magnetic field was changed from 0 to 10 kOe at room temperature, which made it possible to measure the saturation magnetization (M_s), a saturation of remanent magnetization (M_r), and coercive force (H_c) for each sample.

In order to detect iron ions, the powder was suspended in deionized water, then subjected to centrifugation (6000 rpm, 5 min) after 0, 0.5, 1, 3, and 24 h. Appropriate ion detection reagents were added to the supernatant after separation. In order to detect Fe^{3+} ions, 200 μL of potassium thiocyanate KSCN (50% solution) and 200 μL of HCl (18.25% solution) was added to 5 mL of supernatant since the reaction between the Fe^{3+} ions and KSCN proceeded in a strongly acidic medium at pH close to 2. Then the solution was kept for 20 min to reach equilibrium, and the absorption spectrum in the region of 490 nm was measured. In order to detect Fe^{2+} ions, 2 mL phenanthroline $\text{C}_{12}\text{H}_8\text{N}_2 \cdot \text{H}_2\text{O}$ (2.5% solution) and 600 μL of ammonium acetate buffer solution (250 mL of NH_4OH and 900 mL of glacial acetic acid) were also added to the 5 mL of supernatant. Further, the solution was also kept for 20 min to reach equilibrium (no color change) and examined in the region of 690 nm. The absorbance was detected by UV–Vis–NIR spectrophotometry (Cary UV–Vis–NIR Spectrophotometer, Agilent Technologies)

3. Results and Discussion

3.1. Microstructure of Iron Nanoparticles

The diffraction patterns of the samples contain narrow and symmetrical peaks indicating the formation of a well-crystallized material for all NPs samples except for ferrihydrite (Figure 1). Ferrihydrite ($5\text{Fe}_2\text{O}_3 \cdot 9\text{H}_2\text{O}$) is weakly crystalline due to a highly hydrated structure.

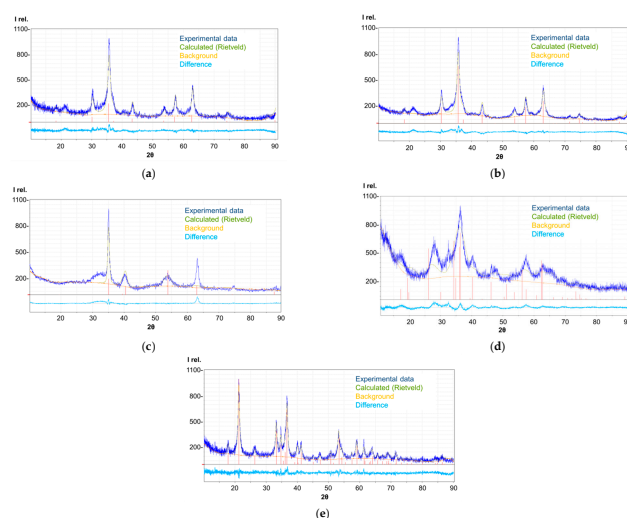


Figure 1. Experimental diffraction patterns of samples: (a) Fe_3O_4 , (b) $\gamma\text{-Fe}_2\text{O}_3$, (c) $\delta\text{-FeOOH}$, (d) $5\text{Fe}_2\text{O}_3 \cdot 9\text{H}_2\text{O}$, (e) $\alpha\text{-FeOOH-Fe}^{2+}$ and the results of their refinement by the Rietveld method.

Quantitative evaluation of XRD data was carried out by the Rietveld method. The main structural parameters of the nanoparticles were determined by using the Crystallography Open Database.

Table 1 presents the lattice parameters of each sample and the Goodness of Fit (GoF)², which is the (R_{WP}/R_{exp})² ratio [28]. The (GoF)² value should approach 1.

Table 1. Quantitative phase analysis after Rietveld method.

Sample	Fe ₃ O ₄	γ-Fe ₂ O ₃	δ-FeOOH	5Fe ₂ O ₃ ·9H ₂ O	α-FeOOH-Fe ²⁺
a, A	8.331	8.344	2.951	5.961	4.609
b, A	-	-	-	-	9.965
c, A	-	-	4.586	8.499	3.022
Structure	Fe _{2.66} O ₄	Fe _{2.56} O ₄	-	-	-
D _{XRD} , nm	6.6 ± 0.2	6.8 ± 0.2	8.1 ± 3.4	3.5 ± 0.5	12.3 ± 2.8
(GoF) ²	1.80	1.10	1.70	1.10	1.20
Composition determined	Fe _{2.66} O ₄	Fe _{2.56} O ₄	δ-FeOOH	5Fe ₂ O ₃ ·9H ₂ O	α-FeOOH

The main phases of all synthesized samples coincide with those predicted, except for Fe₃O₄. The lattice parameters of Fe₃O₄ and γ-Fe₂O₃ samples obtained in this work are smaller than those known for magnetite (ICDD–PDF 19–629) but larger than for maghemite (ICDD–PDF 39–1346) due to the formation of nonstoichiometric Fe_{3–δ}O₄. The sizes of coherent scattering regions (CSRs) are presented in Table 1. According to Gorski et al., 2010 [29], for magnetite with an ideal Fe²⁺ content (assuming the Fe₃O₄ formula), the mineral phase is known as stoichiometric magnetite (x = 0.50). As magnetite becomes oxidized, the Fe²⁺/Fe³⁺ ratio (Formula (1)) decreases (x < 0.50), with this form denoted as nonstoichiometric or partially oxidized magnetite. The stoichiometry can easily be converted to the following relationship:

$$x = \frac{\text{Fe}^{2+}}{\text{Fe}^{3+}} = \frac{1 - 3\delta}{2 + 2\delta} \quad (1)$$

Finally, the composition of crystalline components of the magnetite and maghemite Fe_{3–δ}O₄ can be assigned as follows: Fe_{2.66}O₄ for magnetite and Fe_{2.56}O₄ for maghemite (Table 1).

The Mössbauer spectra (MS) of Fe₃O₄ and γ-Fe₂O₃ samples are similar to each other and have a strong temperature dependence characteristic of nanosized particles in the superparamagnetic state [30]. At a temperature of 295 K, the spectra are a combination of an intense paramagnetic doublet and a strongly broadened and distorted sextet, described by a polymodal probability function of the distribution of magnetic fields, as shown in Figure 2.

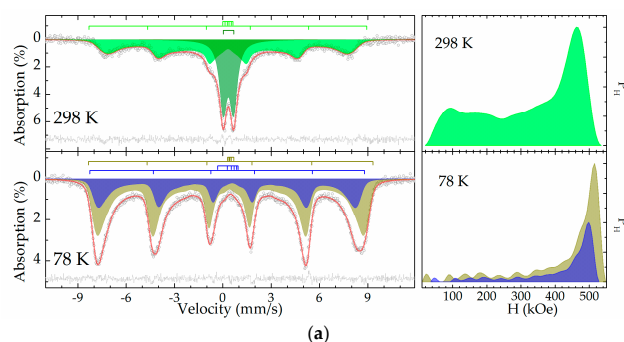


Figure 2. Cont.

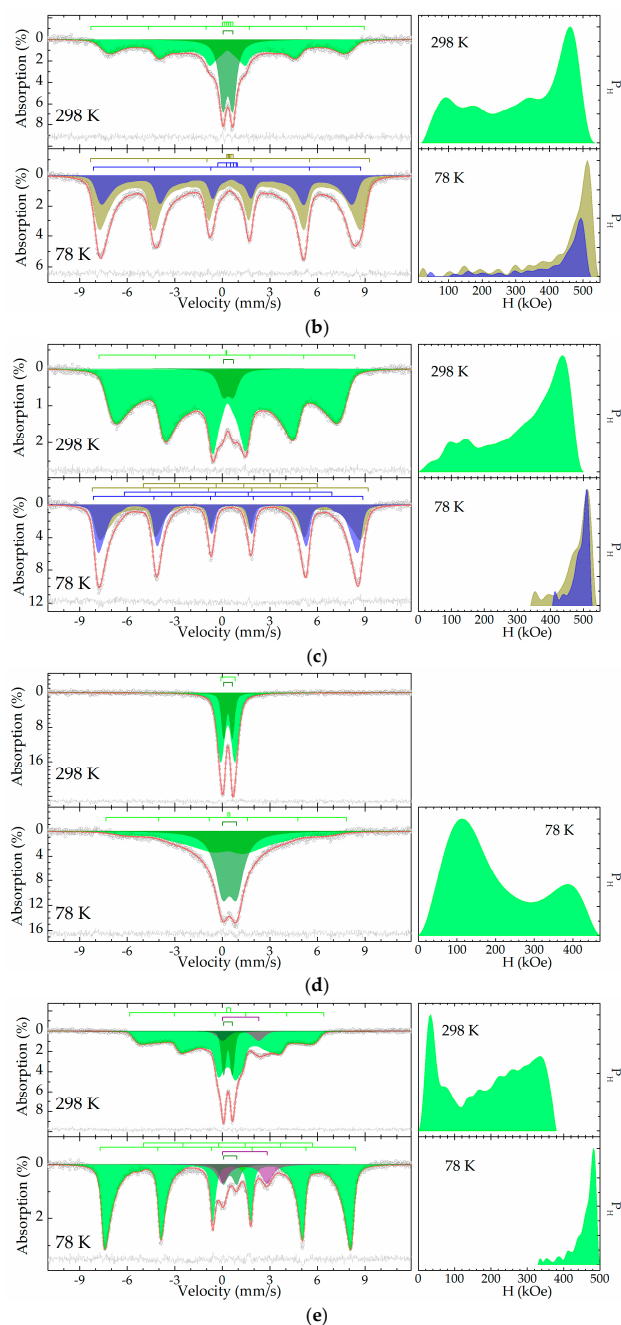


Figure 2. Mössbauer spectra at various temperatures, description models, and distribution of the probability function for magnetic fields of samples: (a) Fe_3O_4 , (b) $\gamma\text{-Fe}_2\text{O}_3$, (c) $\delta\text{-FeOOH}$, (d) $5\text{Fe}_2\text{O}_3 \cdot 9\text{H}_2\text{O}$, (e) $\alpha\text{-FeOOH-Fe}^{2+}$.

At a sample temperature of 78 K, the spectra contain only the resonance lines of the sextet, which are also distorted and asymmetric both in intensity and width, which indicates their composite character. Indeed, the low-temperature spectra of both samples can be satisfactorily described only by a combination of two sextets described by unimodal probability functions for the distribution of magnetic fields with the same profiles and an area ratio of 1/2, which correspond to two iron-containing sub-lattices of the same phase in accordance with the Figure 2. It is obvious that the number of subspectra, the ratio of their areas, and the values of hyperfine parameters allow us to attribute them to the oxidized form of iron oxide with the spinel structure—maghemite [31,32].

Room temperature of the Mössbauer spectra for the $\delta\text{-FeOOH}$ sample represents continuous absorption over a wide range of velocities, which can be described by a sextet

using a single probability function distribution for a set of Mössbauer hyperfine parameters (isomer shift, quadrupole splitting, and magnetic field) and an additional paramagnetic doublet indicated in Table 2. Cooling the sample to the boiling point of liquid nitrogen leads to the transformation of the MS to a practically symmetrical sextet, which can be described by a combination of two sextets described by unimodal probability distribution functions of magnetic fields with the same profiles and an area ratio of 1/1, which correspond to two iron-containing sublattices of the same phase, as shown in Figure 2. The nature of the temperature dependences of hyperfine parameters and their values allow us to attribute them to ferrosyhyte— δ -FeOOH [33–35].

Table 2. Results of non-model description of the Mössbauer spectra of samples.

Temperature, K		296					78				
Sample	#	δ (δ_{ext}) ¹	Δ (Δ_{ext}) mm/s	Γ_{exp}	H_{ext} kOe	S# %	δ (δ_{ext})	Δ mm/s	Γ_{exp}	H_{ext} kOe	S# %
Fe ₃ O ₄	1	0.317	−0.02	0.42	464	64.8	0.445	0.08	0.45	514	66.7
	2	0.351	0.640	0.55	-	35.2	0.437	−0.35	0.50	498	33.3
γ -Fe ₂ O ₃	1	0.330	0.00	0.43	461	67.7	0.447	0.069	0.48	513	66.7
	2	0.353	0.617	0.56	-	32.3	0.444	−0.31	0.48	493	33.3
δ -FeOOH	1	(0.358)	(−0.162)	0.48	437	94	0.489	0.02	0.46	512	50.0
	2	0.38	0.64	0.75	-	6	0.479	−0.24	0.42	510	50.0
5Fe ₂ O ₃ ·9H ₂ O	1	0.351	0.90	0.57	-	72	(0.32)	−0.13	1.08	387	49
	2	0.361	0.55	0.34	-	28	(0.38)	0.879	1.08	114	51
α -FeOOH-Fe ²⁺	1	0.391	−0.233	0.343	335	80.8	0.473	−0.25	0.295	483	82.4
	2	0.361	0.547	0.343	-	12.6	0.49	0.83	0.56	-	7.1
	3	1.16	2.28	0.82	-	6.6	1.42	2.81	0.82	-	10.5

¹ δ is the isomeric shift, Δ is the quadrupole splitting, Γ_{exp} is the linewidth, H_{ext} is the hyperfine magnetic field for the extremum of the mode distribution functions, and S# is the relative area of the subspectrum#.

At a temperature of 295 K, the Mössbauer spectrum of the 5Fe₂O₃·9H₂O sample is paramagnetic, in accordance with Figure 2, and can be satisfactorily described by a pair of doublets corresponding to iron (+3) atoms in the octahedral oxygen environment indicated in Table 2 [36]. As the temperature decreases to 78 K, the width of the doublet increases significantly with the formation of extended “wings”, which can be conditionally described by the broadened doublet and the distribution of the probability function of the isomer shift, and the magnetic field strength for the sextet, as shown in Figure 2. The calculated hyperfine MS parameters can correspond to akageneite— β -FeOOH [33,37] and ordered ferrihydrite [38,39].

The MS of the α -FeOOH-Fe²⁺ sample at different temperatures can be satisfactorily described by a superposition of two doublets and a sextet described by the probability function of the distribution of magnetic fields shown in Figure 2. The doublet with a larger isomer shift and quadrupole splitting (#3, Table 2) obviously corresponds to hydrated iron ions (+2) [36,40], and the doublet with a smaller isomeric shift and quadrupole splitting (#2, Table 2) to iron (+3) ions in an octahedral oxygen environment [36]. The temperature dependence of the hyperfine parameters for the ferromagnetic part of the spectrum (#1, Table 2) allows for unambiguously attributing it to goethite— α -FeOOH with Fe²⁺ [31,35,41]. Furthermore, the cipher α -FeOOH-Fe²⁺ for α -FeOOH.

3.2. Magnetic Characteristics of Samples

The magnetization curves of the samples are shown in Figure 3. The absence of magnetic hysteresis in the Fe₃O₄ and γ -Fe₂O₃ samples indicates the production of superparamagnetic particles. It can be seen from the hysteresis curves that the δ -FeOOH and 5Fe₂O₃·9H₂O samples demonstrate linear behavior in the measured range of the magnetic field and exhibit paramagnetic properties. The α -FeOOH-Fe²⁺ sample exhibits non-linear

behavior near $H = 0$. Such behavior may indicate an additional magnetic phase or indicate the presence of unbalanced spins in the sample [42].

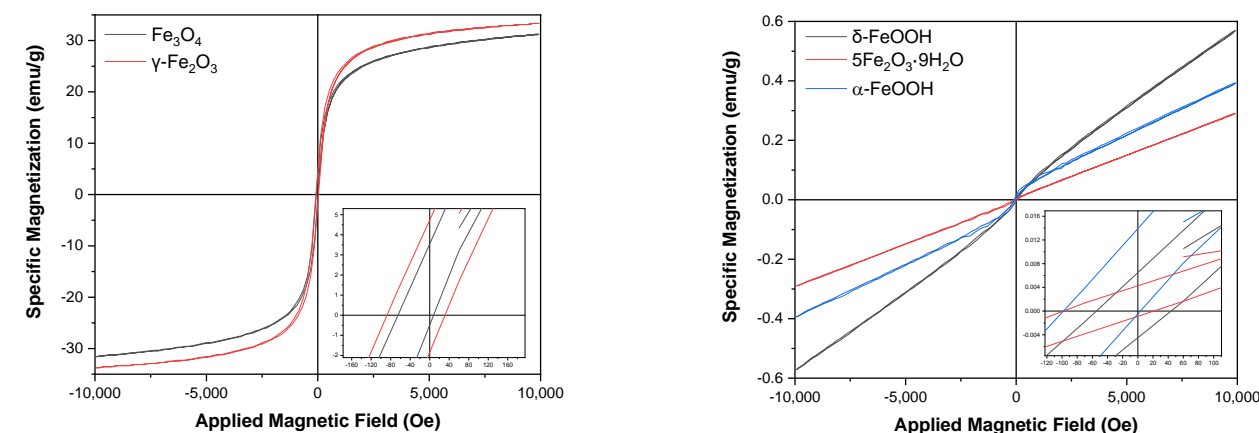


Figure 3. Magnetization curves of iron NP.

The results of the study of the magnetic characteristics of the samples in accordance with Table 3 indicate that the samples Fe_3O_4 and $\gamma\text{-Fe}_2\text{O}_3$ have the highest value of saturation magnetization. All samples have low magnetic characteristics compared to the data [43–47].

Table 3. Magnetic parameters.

Sample	Magnetization Saturation (M_s) emu/g	Residual Magnetization (M_r) emu/g	Coercive Power (H_c) Oe
Fe_3O_4	31.5	2.0	39.5
$\gamma\text{-Fe}_2\text{O}_3$	33.5	3.28	59.0
$\delta\text{-FeOOH}$	0.54	0.006	50.2
$5\text{Fe}_2\text{O}_3 \cdot 9\text{H}_2\text{O}$	0.28	0.002	64.8
$\alpha\text{-FeOOH-Fe}^{2+}$	0.41	0.007	50.1

The high values of the coercive force of the samples $\delta\text{-FeOOH}$, $5\text{Fe}_2\text{O}_3 \cdot 9\text{H}_2\text{O}$ and $\alpha\text{-FeOOH}$ compared to Fe_3O_4 and $\gamma\text{-Fe}_2\text{O}_3$ can be associated with an asymmetric crystal lattice, as shown by XRD, which also increases the magnetic exchange anisotropy. According to Mössbauer spectroscopy data, the $5\text{Fe}_2\text{O}_3 \cdot 9\text{H}_2\text{O}$ sample can contain the $\beta\text{-FeOOH}$ phase, and the $\alpha\text{-FeOOH-Fe}^{2+}$ sample contains hydrated iron ions (+2) and iron ions (+3) in an octahedral oxygen environment, which also increases the magnetic exchange anisotropy.

3.3. Textural Characteristics

Adsorption/desorption isotherms of nitrogen for iron nanoparticles are presented in Figure 4. All samples are characterized by type IV isotherms according to the classification, which indicates the occurrence of polymolecular adsorption and the presence of capillary condensation in mesopores. Samples of Fe_3O_4 , $\gamma\text{-Fe}_2\text{O}_3$, and $\delta\text{-FeOOH}$ have an H1-type hysteresis loop associated with the filling of mesopores due to capillary condensation. The $\alpha\text{-FeOOH-Fe}^{2+}$ sample has a hysteresis loop of the H4 type. The $5\text{Fe}_2\text{O}_3 \cdot 9\text{H}_2\text{O}$ has a hysteresis loop of the H2(a) type with a corpuscular structure, but the distribution and shape of the pores are inhomogeneous in this case. The presence of a steep rise in the isotherm at low pressures may indicate the presence of micropores.

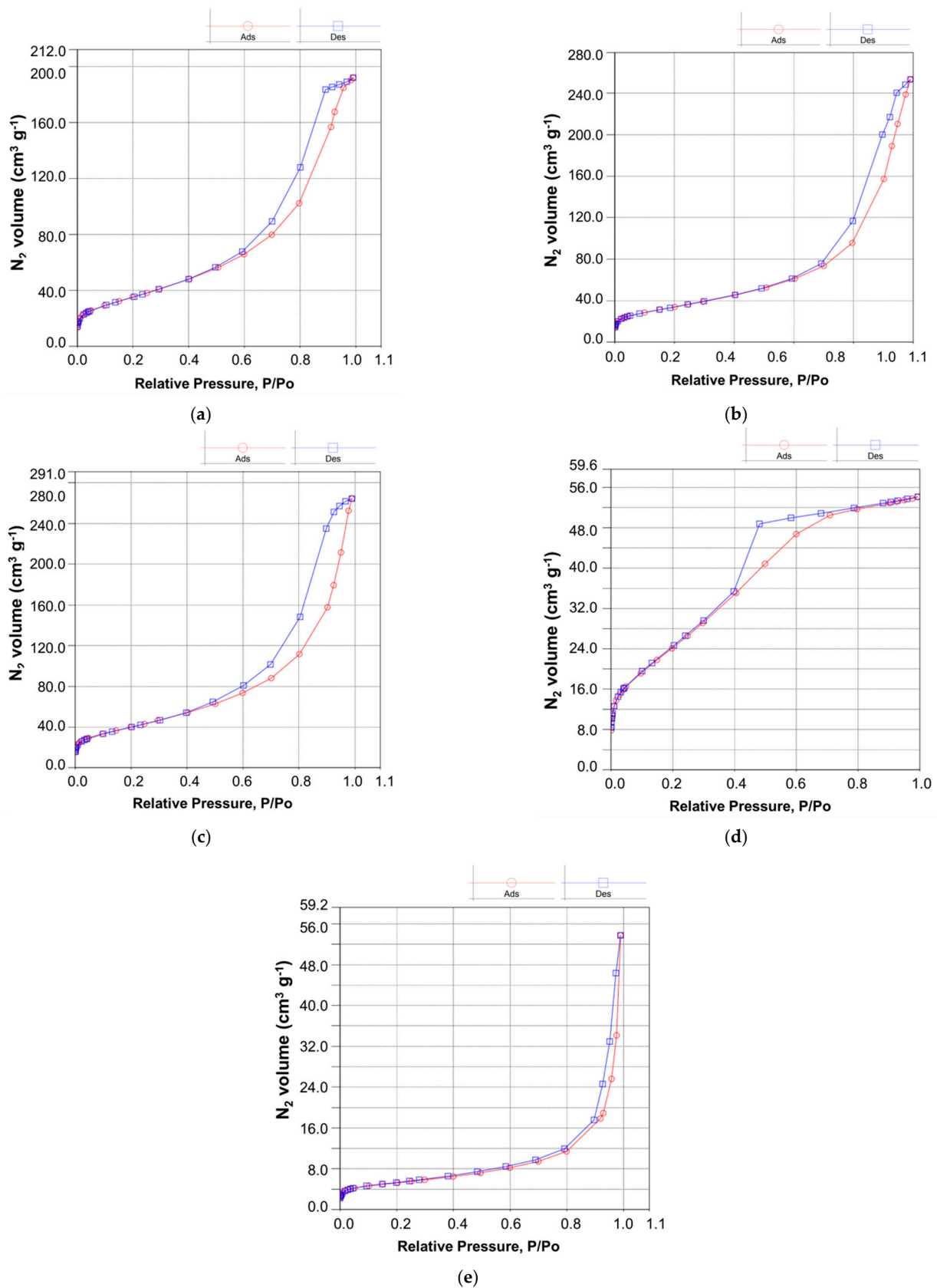


Figure 4. Isotherms of low-temperature (77 K) nitrogen adsorption/desorption of samples: (a) Fe_3O_4 , (b) $\gamma-Fe_2O_3$, (c) $\delta-FeOOH$, (d) $5Fe_2O_3 \cdot 9H_2O$, (e) $\alpha-FeOOH-Fe^{2+}$.

Data for the specific surface area of the samples by the BET method and the average pore diameter by the BJH method (Table 4 and see Supplementary Materials, Figure S1) demonstrated that all NPs have a significant decrease in the specific surface area (SSA), compared with the data [25,48–50]. Samples of ferroxhyte and ferrihydrite showed a significant decrease in specific surface area compared to the data [25,47] as a result of the synthesis conditions we used.

Table 4. Textural parameters.

Sample	BET ¹		BJH ²	
	SSA m ² /g	Pore Volume cm ³ /g	Pore Volume cm ³ /g	Pore Diameter nm
Fe ₃ O ₄	130.9	0.30	0.29	8.86
γ-Fe ₂ O ₃	123.0	0.39	0.39	8.71
δ-FeOOH	147.5	0.41	0.41	8.94
5Fe ₂ O ₃ ·9H ₂ O	97.0	0.084	0.056	3.54
α-FeOOH-Fe ²⁺	18.8	0.083	0.080	23.8

¹ Brunauer–Emmett–Teller, ² Barrett–Joyner–Halenda.

3.4. Iron Ions Release

Various iron-based nanomaterials have been widely investigated to induce ferroptosis for the proposed reason that the Fenton reaction between iron ions and tumor cellular H₂O₂ could generate reactive oxygen species (ROS), which further causes the accumulation of lipid peroxidation [8,13,51–55]. Iron-containing compounds such as magnetite [12,56], maghemite [5], and iron salts [51,52] were used as sources of Fe²⁺ and Fe³⁺ as a catalyst for the Fenton reaction. A disadvantage of the latter is the impossibility of the application of a magnetic field for the target drug delivery.

UV-Vis spectroscopy was used to demonstrate the kinetics and concentration of the released Fe²⁺ and Fe³⁺ from nanoparticles Fe₃O₄, γ-Fe₂O₃, δ-FeOOH, 5Fe₂O₃·9H₂O, α-FeOOH-Fe²⁺ (see Supplementary Materials, Figure S2). The concentrations of iron ions were recalculated per 1 g of the iron.

According to complexometric results (Figure 5), α-FeOOH-Fe²⁺ released both Fe²⁺ and Fe³⁺, while δ-FeOOH, Fe₃O₄, γ-Fe₂O₃, and 5Fe₂O₃·9H₂O released only Fe³⁺. In this case, the concentration of ions released by nanoparticles differs. Thus, the concentration of ions released by all nanoparticles, except α-FeOOH-Fe²⁺, reached 9.1 mg/L for Fe³⁺, which makes them preferable for controlling the catalysis of the Fenton reaction. While the high concentration of iron ions to 90 mg/L for Fe³⁺ and 316 mg/L for Fe²⁺ released from α-FeOOH-Fe²⁺ can be used in case of aid therapy. Moreover, the kinetics of the release of the total concentration of ions is similar to all iron-containing compounds: the concentration of ions in the solution increases within 3 h. After 24 h, a decrease in the concentration of ions is observed, which may indicate the adsorption of ions from the solution onto the NPs' surface [57].

The estimated release from composites produced by the lowest amount of Fe³⁺ was released from glass compositions with the highest Fe₂O₃ content [5]. It can be suggested that the release of Fe³⁺ was dictated by the durability of the glass rather than the amount of Fe³⁺ available in the glass. The character of the release of ions is similar to the one from the nanoparticles we studied: the authors observed an increase in the concentration of the released nanoparticles within 24 h and then a significant, down to 0 mg/L, decrease in the concentration within 95 h for nanoparticles with different concentrations of Fe₂O₃. In our case, the low concentration of released ions at pH close to neutral (6.6 for γ-Fe₂O₃ and 7.0 for Fe₃O₄) can be associated with the formation of Fe³⁺ hydroxocomplexes under these conditions. At the same time, the low concentration of released ions makes the usage of magnetic nanoparticles more controllable, for example, by adding H₂O₂. The high release

of ions from α -FeOOH-Fe²⁺ can lead to a speedy Fenton reaction that can be used for aid therapy cases. A comparison of the concentration of Fe³⁺ released by Fe₃O₄ and γ -Fe₂O₃ showed that the nanoparticles release approximately the same concentration of ferric ions into the solution, which confirms the identity of their structural parameters shown by XRD and surrounding local data for Fe atoms/ions shown by Mössbauer spectroscopy. The concentration of Fe²⁺ released by Fe₃O₄ may be too low to be detected by the method used, or Fe²⁺ at a pH close to neutral (6.6 for γ -Fe₂O₃ and 7.0 for Fe₃O₄) is rapidly oxidized to Fe³⁺.

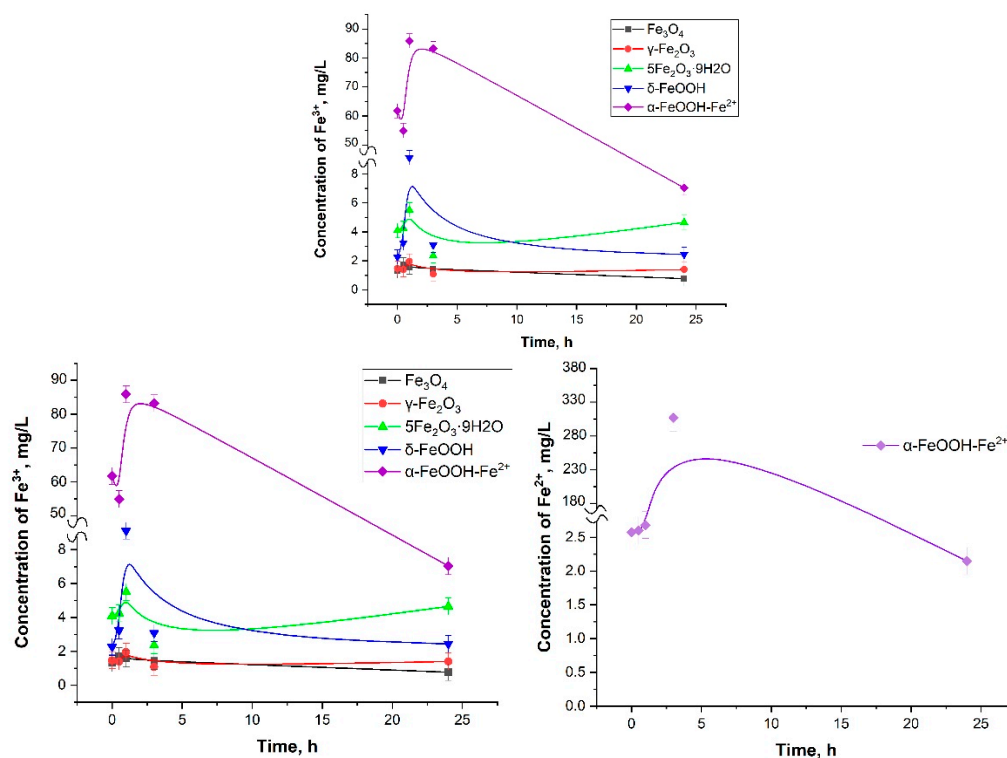


Figure 5. Fe²⁺ and Fe³⁺ ion release kinetics from Fe₃O₄, γ -Fe₂O₃, δ -FeOOH, 5Fe₂O₃·9H₂O, α -FeOOH nanoparticles (Fe₃O₄ pH 7, γ -Fe₂O₃ pH 6.6 α -FeOOH-Fe²⁺ pH 6.9 δ -FeOOH pH 6.7, 5Fe₂O₃·9H₂O pH 6.9) (see Supplementary Materials Figure S2).

Comparative assessment of the concentration of ions released by various iron-containing materials is complicated by several factors: (1) different methods of assessment (ICP-MS or UV-Vis spectroscopy with different reagents), which imply different errors, and (2) no information about the processing of primary data in terms of iron content in the sample, the concentration of trace elements, etc.

Evaluation of ions released for δ -FeOOH revealed that the concentration of ferrous ions increases strictly after three hours of suspension: from 2.2 mg/L to 9.1 mg/L for Fe³⁺. Further, the concentration of ions in the solution decreases to 2.4 mg/L for Fe³⁺.

The study of 5Fe₂O₃·9H₂O as a source of iron ions showed that the concentration of Fe³⁺ in the solution remains practically unchanged during the first hour of the measurements (4–5.4 mg/L), then decreases to 2.3 mg/L and increases again to 4.6 mg/L after 24 h. These processes may indicate ongoing adsorption and desorption of ions from the surface of nanoparticles.

Withal, α -FeOOH-Fe²⁺ is released at least 50 times more Fe³⁺ and 150 times more Fe²⁺ than the rest of the studied compounds, although its surface area was 18.2 m²/g, which is much less than the surface area of the other compounds. The high concentration of Fe²⁺ in the solution is explained by the modified synthesis of Fe²⁺-doped α -FeOOH in ambient conditions resulting in the Fe²⁺ presence. The concentration of Fe³⁺ increased from ~60 mg/L to ~80 mg/L after an hour and then decreased to 35.1 mg/L after a day

of observation; the concentration of Fe^{2+} increased sharply after 3 h from ~180 mg/L to 316 mg/L and then also decreased to 150 mg/L. In general, goethite released ~3 times more ferrous ions than ferric iron during the day.

4. Conclusions

The estimation of the most prospective iron oxide nanoparticles in terms of release of $\text{Fe}^{2+}/\text{Fe}^{3+}$, surface, and magnetic characteristics was performed in order to further utilize them as mediators for the Fenton reaction. The crystal structure and oxygen local environment of all samples that were analyzed using XRD and Mossbauer spectroscopy, respectively, correspond to the mixture of Fe_3O_4 and $\gamma\text{-Fe}_2\text{O}_3$, $\gamma\text{-Fe}_2\text{O}_3$, $\delta\text{-FeOOH}$, $5\text{Fe}_2\text{O}_3\cdot 9\text{H}_2\text{O}$, and Fe^{2+} -doped $\alpha\text{-FeOOH}$ with Fe^{2+} . Nanoparticles of Fe_3O_4 and $\gamma\text{-Fe}_2\text{O}_3$ synthesized in ambient conditions are a mixture of magnetite and maghemite with composition as $\text{Fe}_{2.66}\text{O}_4$, and goethite with Fe^{2+} , respectively. The saturation magnetization for Fe_3O_4 (31.6 emu/g) and $\gamma\text{-Fe}_2\text{O}_3$ (33.8 emu/g), as well as the surface area of these particles (130 and 123 m^2/g), make it possible to consider them as promising magnetically controlled carriers. A low release of $\text{Fe}^{2+}/\text{Fe}^{3+}$ from nanoparticles during the first three hours makes them preferable for controlling the catalysis of the Fenton reaction. Whereas a high concentration of iron ions to 90 mg/L for Fe^{3+} and 316 mg/L for Fe^{2+} released from complex $\alpha\text{-FeOOH}\text{-Fe}^{2+}$ allows it to be utilized as an aid therapy agent. Thus, primary results on $\text{Fe}^{2+}/\text{Fe}^{3+}$ release by iron oxide and hydroxide nanoparticles will provide information to form a whole new class of prospective preparations that will express maximal efficacy and specificity in ferroptosis-inducing systems.

Supplementary Materials: The following supporting information can be downloaded at: <https://www.mdpi.com/article/10.3390/magnetochemistry9010003/s1>, Figure S1: Pore size distribution from a BJH model of samples: (a) Fe_3O_4 , (b) $\gamma\text{-Fe}_2\text{O}_3$, (c) $\delta\text{-FeOOH}$, (d) $5\text{Fe}_2\text{O}_3\cdot 9\text{H}_2\text{O}$, (e) $\alpha\text{-FeOOH}$; Figure S2: UV-Vis spectra of Fe^{2+} and Fe^{3+} ion release kinetics (a) Fe_3O_4 , (b) $\gamma\text{-Fe}_2\text{O}_3$, (c) $\delta\text{-FeOOH}$, (d) $5\text{Fe}_2\text{O}_3\cdot 9\text{H}_2\text{O}$, (e) $\alpha\text{-FeOOH}$ nanoparticles.

Author Contributions: Conceptualization, K.K. and L.B.; methodology, L.B. and K.K.; software, L.B. and L.T.; validation, N.T. and G.D.; formal analysis, D.P.; investigation, A.D., M.P., L.B. and D.P.; resources, G.D. and N.T.; data curation, S.J.; writing—original draft preparation, writing—review and editing, K.K. and L.B.; supervision, S.J. All authors have read and agreed to the published version of the manuscript.

Funding: This research was funded by Russian Science Foundation, N 22-73-10222.

Institutional Review Board Statement: Not applicable.

Informed Consent Statement: Not applicable.

Data Availability Statement: Not applicable.

Conflicts of Interest: The authors declare no conflict of interest.

References

1. Shams, M.; Owczarczak, B.; Manderscheid-Kern, P.; Bellnier, D.A.; Gollnick, S.O. Development of photodynamic therapy regimens that control primary tumor growth and inhibit secondary disease. *Cancer Immunol. Immunother.* **2014**, *64*, 287–297. [[CrossRef](#)] [[PubMed](#)]
2. Efimova, I.; Catanzaro, E.; Van der Meer, L.; Turubanova, V.D.; Hammad, H.; Mishchenko, T.A.; Vedunova, M.V.; Fimognari, C.; Bachert, C.; Coppieters, F.; et al. Vaccination with early ferroptotic cancer cells induces efficient antitumor immunity. *J. Immunother. Cancer.* **2020**, *8*, e001369. [[CrossRef](#)] [[PubMed](#)]
3. Szatrowski, T.P.; Nathan, C.F. Production of large amounts of hydrogen peroxide by human tumor cells. *Cancer Res.* **1991**, *51*, 794–798. [[PubMed](#)]
4. Dan, Q.; Hu, D.; Ge, Y.; Zhang, S.; Li, S.; Gao, D.; Sheng, Z. Ultrasmall theranostic nanozymes to modulate tumor hypoxia for augmenting photodynamic therapy and radiotherapy. *Biomater. Sci.* **2020**, *107*, 2411–2502. [[CrossRef](#)]
5. El-Fiqi, A.; Kim, H.-W. Iron ions-releasing mesoporous bioactive glass ultrasmall nanoparticles designed as ferroptosis-based bone cancer nanotherapeutics: Ultrasonic-coupled sol-gel synthesis, properties and iron ions release. *Mater. Lett.* **2021**, *294*, 129759. [[CrossRef](#)]

6. Li, J.; Xiong, Z.; Yu, Y.; Wang, X.; Zhou, H.; Huang, B.; Lai, B. Efficient degradation of carbamazepine by electro-Fenton system without any extra oxidant in the presence of molybdate: The role of slow release of iron ions. *Appl. Catal. B Environ.* **2021**, *298*, 120506. [[CrossRef](#)]
7. Yang, Y.; Zuo, S.; Li, L.; Kuang, X.; Li, J.; Sun, B.; Sun, J. Iron-doxorubicin prodrug loaded liposome nanogenerator programs multimodal ferroptosis for efficient cancer therapy. *Asian J. Pharm. Sci.* **2021**, *16*, 784–793. [[CrossRef](#)]
8. Shen, Z.; Song, J.; Yung, B.C.; Zhou, Z.; Wu, A.; Chen, X. Emerging strategies of cancer therapy based on ferroptosis. *Adv. Mater.* **2018**, *30*, 1704007. [[CrossRef](#)]
9. Meng, X.; Deng, J.; Liu, F.; Guo, T.; Liu, M.; Dai, P.; Zhao, Y. Triggered all-active metal organic framework: Ferroptosis machinery contributes to the apoptotic photodynamic antitumor therapy. *Nano Lett.* **2019**, *19*, 7866–7876. [[CrossRef](#)]
10. Shan, X.; Li, S.; Sun, B.; Chen, Q.; Sun, J.; He, Z.; Luo, C. Ferroptosis-driven nanotherapeutics for cancer treatment. *J. Control Release* **2020**, *319*, 322–332. [[CrossRef](#)]
11. An, Q.; Sun, C.; Li, D.; Xu, K.; Guo, J.; Wang, C. Peroxidase-like activity of Fe₃O₄@carbon nanoparticles enhances ascorbic acid-induced oxidative stress and selective damage to PC-3 prostate cancer cells. *ACS Appl. Mater. Interfaces* **2013**, *5*, 13248–13257. [[CrossRef](#)]
12. Huo, M.; Wang, L.; Chen, Y.; Shi, J. Tumor-selective catalytic nanomedicine by nanocatalyst delivery. *Nat. Commun.* **2017**, *8*, 357. [[CrossRef](#)]
13. Zheng, D.-W.; Lei, Q.; Zhu, J.-Y.; Fan, J.-X.; Li, C.-X.; Li, C.; Xu, Z.; Cheng, S.-X.; Zhang, X.-Z. Switching apoptosis to ferroptosis: Metal-organic network for high-efficiency anticancer therapy. *Nano Lett.* **2016**, *17*, 284–291. [[CrossRef](#)]
14. Liang, Y.; Zhang, L.; Peng, C.; Zhang, S.; Chen, S.; Qian, X.; Luo, W.; Dan, Q.; Ren, Y.; Li, Y.; et al. Tumor microenvironments self-activated nanoscale metal-organic frameworks for ferroptosis based cancer chemodynamic/photothermal/chemo therapy. *Acta Pharm. Sin. B* **2021**, *11*, 3231–3243. [[CrossRef](#)]
15. Minotti, G.; Aust, S.D. The role of iron in the initiation of lipid peroxidation. *Chem. Phys. Lipids* **1987**, *44*, 191–208. [[CrossRef](#)]
16. He, Y.-J.; Liu, X.-Y.; Xing, L.; Wan, X.; Chang, X.; Jiang, H.-L. Fenton reaction-independent ferroptosis therapy via Glutathione and iron redox couple sequentially triggered lipid peroxide generator. *Biomaterials* **2020**, *241*, 119911. [[CrossRef](#)]
17. Hah, H.Y.; Gray, S.; Johnson, C.E.; Johnson, J.A.; Kolesnichenko, V.; Kucheryavy, P.; Goloverda, G. Mössbauer spectroscopy of superparamagnetic Fe₃O₄ nanoparticles. *J. Magn. Magn. Mater. J.* **2021**, *539*, 168382. [[CrossRef](#)]
18. Tuutijärvi, T.; Lu, J.; Sillanpää, M.; Chen, G. As(V) adsorption on maghemite nanoparticles. *J. Hazard. Mater.* **2009**, *166*, 1415–1420. [[CrossRef](#)]
19. Faria, M.C.S.; Rosemberg, R.S.; Bomfeti, C.A.; Monteiro, D.S.; Barbosa, F.; Oliveira, L.C.A.; Rodrigues, J.L. Arsenic removal from contaminated water by ultrafine δ-FeOOH adsorbents. *Chem. Eng. J.* **2014**, *237*, 47–54. [[CrossRef](#)]
20. Patrat, G.; de Bergevin, F.; Pernet, M.; Joubert, J.C. Structure locale de δ-FeOOH. *Acta. Crystallogr. B. Struct.* **1983**, *39*, 165–170. [[CrossRef](#)]
21. Eusterhues, K.; Rennert, T.; Knicker, H.; Kögel-Knabner, I.; Totsche, K.U.; Schwertmann, U. Fractionation of organic matter due to reaction with ferrihydrite: Coprecipitation versus adsorption. *Environ. Sci. Technol.* **2011**, *45*, 527–533. [[CrossRef](#)] [[PubMed](#)]
22. Lv, J.; Zhang, S.; Wang, S.; Luo, L.; Cao, D.; Christie, P. Molecular-scale investigation with ESI-FT-ICR-MS on fractionation of dissolved organic matter induced by adsorption on iron oxyhydroxides. *Envi Environ. Sci. Technol.* **2016**, *50*, 2328–2336. [[CrossRef](#)] [[PubMed](#)]
23. Tipping, E. The adsorption of aquatic humic substances by iron oxides. *Geochim. Cosmochim. Acta.* **1981**, *45*, 191–199. [[CrossRef](#)]
24. Elmore, W.C. Ferromagnetic colloid for studying magnetic structures. *Phys. Rev.* **1938**, *54*, 309–310. [[CrossRef](#)]
25. Pinto, I.S.X.; Pacheco, P.H.V.V.; Coelho, J.V.; Lorençon, E.; Ardisson, J.D.; Fabris, J.D.; Pereira, M.C. Nanostructured δ-FeOOH: An efficient Fenton-like catalyst for the oxidation of organics in water. *Appl. Catal. B: Environ.* **2012**, *119–120*, 175–182. [[CrossRef](#)]
26. Zhang, P.; Liu, A.; Huang, P.; Min, L.; Sun, H. Sorption and molecular fractionation of biochar-derived dissolved organic matter on ferrihydrite. *J. Hazard. Mater.* **2020**, *392*, 122260. [[CrossRef](#)]
27. Lowry, G.V.; Johnson, K.M. Congener-specific dechlorination of dissolved PCBs by microscale and nanoscale zerovalent iron in a water/methanol solution. *Environ. Sci. Technol.* **2004**, *38*, 5208–5216. [[CrossRef](#)]
28. Toby, B.H. R factors in Rietveld analysis: How good is good enough? *Powder Diffr.* **2006**, *21*, 67–70. [[CrossRef](#)]
29. Gorski, C.A.; Scherer, M.M. Determination of nanoparticulate magnetite stoichiometry by Mossbauer spectroscopy, acid dissolution, and powder X-ray diffraction: A critical review. *Am. Mineral.* **2010**, *95*, 1017–1026. [[CrossRef](#)]
30. Yurkov, G.Y.; Shashkeev, K.A.; Kondrashov, S.V.; Popkov, O.V.; Shcherbakova, G.I.; Zhigalov, D.V.; Koksharov, Y.A. Synthesis and magnetic properties of cobalt ferrite nanoparticles in polycarbosilane ceramic matrix. *J. Alloys Compd.* **2016**, *686*, 421–430. [[CrossRef](#)]
31. Pankratov, D.A.; Anuchina, M.M.; Spiridonov, F.M.; Krivtsov, G.G. Fe₃—δO₄ Nanoparticles synthesized in the presence of natural polyelectrolytes. *Crystallogr. Rep.* **2020**, *65*, 393–397. [[CrossRef](#)]
32. Pankratov, D.A.; Anuchina, M.M. Nature-inspired synthesis of magnetic non-stoichiometric Fe₃O₄ nanoparticles by oxidative in situ method in a humic medium. *Mater. Chem. Phys.* **2019**, *231*, 216–224. [[CrossRef](#)]
33. Oh, S.J.; Cook, D.C.; Townsend, H.E. Characterization of iron oxides commonly formed as corrosion products on steel. *Hyperfine Interact* **1998**, *112*, 59–66. [[CrossRef](#)]
34. Polyakov, A.Y.; Goldt, A.E.; Sorkina, T.A.; Perminova, I.V.; Pankratov, D.A.; Goodilin, E.A.; Tretyakov, Y.D. Constrained growth of anisotropic magnetic δ-FeOOH nanoparticles in the presence of humic substances. *CrystEngComm* **2012**, *14*, 8097. [[CrossRef](#)]

35. Polyakov, A.Y.; Sorkina, T.A.; Goldt, A.E.; Pankratov, D.A.; Perminova, I.V.; Goodilin, E.A. Mössbauer spectroscopy of frozen solutions as a stepwise control tool in preparation of biocompatible humic-stabilized ferroxhyte nanoparticles. *Hyperfine Interact* **2013**, *219*, 113–120. [[CrossRef](#)]
36. Pankratov, D.A. Mössbauer study of oxo derivatives of iron in the $\text{Fe}_2\text{O}_3\text{-Na}_2\text{O}_2$ system. *Inorg. Mater.* **2013**, *50*, 82–89. [[CrossRef](#)]
37. Valeev, D.; Pankratov, D.; Shoppert, A.; Sokolov, A.; Kasikov, A.; Mikhailova, A.; Salazar-Concha, C.; Rodionov, I. Mechanism and kinetics of iron extraction from high silica boehmite–kaolinite bauxite by hydrochloric acid leaching. *Trans. Nonferrous Met. Soc. China* **2021**, *31*, 3128–3149. [[CrossRef](#)]
38. Zimbovskaya, M.M.; Polyakov, A.Y.; Volkov, D.S.; Kulikova, N.A.; Lebedev, V.A.; Pankratov, D.A.; Perminova, I.V. Foliar application of humic-stabilized nanoferrihydrite resulted in an increase in the content of iron in wheat leaves. *Agronomy* **2020**, *10*, 1891. [[CrossRef](#)]
39. Cieschi, M.T.; Polyakov, A.Y.; Lebedev, V.A.; Volkov, D.S.; Pankratov, D.A.; Veligzhanin, A.A.; Lucena, J.J. Eco-friendly iron-humic nanofertilizers synthesis for the prevention of iron chlorosis in soybean (*Glycine max*) grown in calcareous soil. *Front. Plant Sci.* **2019**, *10*, 413. [[CrossRef](#)]
40. Rostovshchikova, T.N.; Smirnov, V.V.; Tsodikov, M.V.; Bukhtenko, O.V.; Maksimov, Y.V.; Kiseleva, O.I.; Pankratov, D.A. Catalytic conversions of chloroolefins over iron oxide nanoparticles 1. Isomerization of dichlorobutenes in the presence of iron oxide nanoparticles immobilized on silicas with different structures. *Russ. Chem. Bull.* **2005**, *54*, 1418–1424. [[CrossRef](#)]
41. Shoppert, A.; Valeev, D.; Diallo, M.M.; Loginova, I.; Beavogui, M.C.; Rakhmonov, A.; Ovchenkov, Y.; Pankratov, D. High-iron bauxite residue (red mud) valorization using hydrochemical conversion of goethite to magnetite. *Materials* **2022**, *15*, 8423. [[CrossRef](#)] [[PubMed](#)]
42. Valezi, D.F.; Carneiro, C.E.A.; Costa, A.C.S.; Paesano, A.; Spadotto, J.C.; Solórzano, I.G.; Di Mauro, E. Weak ferromagnetic component in goethite ($\alpha\text{-FeOOH}$) and its relation with microstructural characteristics. *Mater. Chem. Phys.* **2020**, *246*, 122851. [[CrossRef](#)]
43. Wang, J.; Sun, J.; Sun, Q.; Chen, Q. One-step hydrothermal process to prepare highly crystalline Fe_3O_4 nanoparticles with improved magnetic properties. *Mater. Res. Bull.* **2003**, *38*, 1113–1118. [[CrossRef](#)]
44. Guivar, J.; Martínez, A.; Anaya, A.; Valladares, L.; Félix, L.; Dominguez, A. Structural and magnetic properties of monophasic maghemite ($\gamma\text{-Fe}_2\text{O}_3$) nanocrystalline powder. *Adv. Nanopart.* **2014**, *3*, 114–121. [[CrossRef](#)]
45. Wu, T.; Li, X.; Fu, Y.; Ding, X.; Li, Z.; Zhu, G.; Fan, J. A highly sensitive and selective fluorescence biosensor for hepatitis C virus DNA detection based on $\delta\text{-FeOOH}$ and exonuclease III-assisted signal amplification. *Talanta* **2019**, *209*, 120550. [[CrossRef](#)]
46. Rani, C.; Tiwari, S.D. Superparamagnetic behavior of antiferromagnetic six lines ferrihydrite nanoparticles. *Phys. B Condens. Matter.* **2017**, *513*, 58–61. [[CrossRef](#)]
47. Pono Ponomar, V.P. Thermomagnetic properties of the goethite transformation during high-temperature treatment. *Miner. Eng.* **2018**, *127*, 143–152. [[CrossRef](#)]
48. Auffan, M.; Achouak, W.; Rose, J.; Roncato, M.-A.; Chanéac, C.; Waite, D.T.; Bottero, J.-Y. Relation between the redox state of iron-based nanoparticles and their cytotoxicity toward *Escherichia coli*. *Environ. Sci. Technol.* **2008**, *42*, 6730–6735. [[CrossRef](#)]
49. Jambor, J.L.; Dutrizac, J.E. Occurrence and constitution of natural and synthetic ferrihydrite, a widespread iron oxyhydroxide. *Chem. Rev.* **1998**, *98*, 2549–2586. [[CrossRef](#)]
50. Gaboriaud, F.; Ehrhardt, J.-J. Effects of different crystal faces on the surface charge of colloidal goethite ($\alpha\text{-FeOOH}$) particles: An experimental and modeling study. *Geochim. Cosmochim. Acta* **2003**, *67*, 967–983. [[CrossRef](#)]
51. Ma, P.A.; Xiao, H.; Yu, C.; Liu, J.; Cheng, Z.; Song, H.; Zhang, X.; Li, C.; Wang, J.; Gu, Z.; et al. Enhanced cisplatin chemotherapy by iron oxide nanocarrier-mediated generation of highly toxic reactive oxygen species. *Nano Lett.* **2017**, *17*, 928–937. [[CrossRef](#)]
52. Shen, Z.; Liu, T.; Li, Y.; Lau, J.; Yang, Z.; Fan, W.; Zhou, Z.; Shi, C.; Ke, C.; Bregadze, V.I.; et al. Fenton-reaction-accelerated magnetic nanoparticles for ferroptosis therapy of orthotopic brain tumors. *ACS Nano* **2018**, *12*, 11355–11365. [[CrossRef](#)]
53. Dong, Z.; Feng, L.; Chao, Y.; Hao, Y.; Chen, M.; Gong, F.; Han, X.; Zhang, R.; Cheng, L.; Liu, Z. Amplification of tumor oxidative stresses with liposomal fenton catalyst and glutathione inhibitor for enhanced cancer chemotherapy and radiotherapy. *Nano Lett.* **2018**, *19*, 805–815. [[CrossRef](#)]
54. Liu, T.; Liu, W.; Zhang, M.; Yu, W.; Gao, F.; Li, C.; Wang, S.B.; Feng, J.; Zhang, X.Z. Ferrous-supply-regeneration nanoengineering for cancer cell specific ferroptosis in combination with imaging-guided photodynamic therapy. *ACS Nano* **2018**, *12*, 12181–12192. [[CrossRef](#)]
55. Bao, W.; Liu, X.; Lv, Y.; Lu, G.H.; Li, F.; Zhang, F.; Liu, B.; Li, D.; Wei, W.; Li, Y. Nanolongan with multiple on-demand conversions for ferroptosis-apoptosis combined anticancer therapy. *ACS Nano* **2019**, *13*, 260–273. [[CrossRef](#)]
56. Fan, J.; Peng, M.; Wang, H.; Zheng, H.; Liu, Z.; Li, C.; Wang, X.; Liu, X.; Cheng, S.; Zhang, X. Engineered bacterial bioreactor for tumor therapy via fenton-like reaction with localized H_2O_2 generation. *Adv. Mater.* **2019**, *31*, 1808278. [[CrossRef](#)]
57. Handler, R.M.; Beard, B.L.; Johnson, C.M.; Scherer, M.M. Atom exchange between aqueous Fe(II) and goethite: An Fe isotope tracer study. *Environ. Sci. Technol.* **2009**, *43*, 1102–1107. [[CrossRef](#)]

Disclaimer/Publisher’s Note: The statements, opinions and data contained in all publications are solely those of the individual author(s) and contributor(s) and not of MDPI and/or the editor(s). MDPI and/or the editor(s) disclaim responsibility for any injury to people or property resulting from any ideas, methods, instructions or products referred to in the content.